atmosphere

MDPI

Article

Can Pre-Storm Errors in the Low-Level Inflow Help Predict Spatial Displacement Errors in MCS Initiation?

Nicholas J. Vertz, William A. Gallus Jr. * and Brian J. Squitieri

Department of Geological and Atmospheric Sciences, Iowa State University, Ames, IA 50011, USA; nvertz@iastate.edu (N.J.V.); brianjs@iastate.edu (B.J.S.)
* Correspondence: wgallus@iastate.edu

Abstract: The Great Plains low-level jet (LLJ) is a contributing factor to the initiation and evolution of nocturnal Mesoscale Convective Systems (MCSs) in the central United States by supplying moisture, warm air advection, and a source of convergence. Thus, the ability of models to correctly depict thermodynamics in the LLJ likely influences how accurately they forecast MCSs. In this study, the Weather Research and Forecasting (WRF) model was used to examine the relationship between spatial displacement errors for initiating simulated MCSs, and errors in forecast thermodynamic variables up to three hours before downstream MCS initiation in 18 cases. Rapid Update Cycle (RUC) analyses in 3 layers below 1500 m above ground level were used to represent observations. Correlations between simulated MCS initiation spatial displacements and errors in the magnitude of forecast thermodynamic variables were examined in regions near and upstream of both observed and simulated MCSs, and were found to vary depending on the synoptic environment. In strongly-forced cases, large negative moisture errors resulted in simulated MCSs initiating further downstream with respect to the low-level flow from those observed. For weakly-forced cases, correlations were weaker, with a tendency for smaller negative moisture errors to be associated with larger displacement errors to the right of the inflow direction for initiating MCSs.

Keywords: mesoscale convective systems; forecast errors; precipitation; low-level jet; numerical weather prediction; convective initiation

Citation: Vertz, N.J.; Gallus, W.A., Jr.; Squitieri, B.J. Can Pre-Storm Errors in the Low-Level Inflow Help Predict Spatial Displacement Errors in MCS Initiation? *Atmosphere* **2021**, *12*, 7. https://dx.doi.org/10.3390/atmos12010007

Received: 21 November 2020
Accepted: 18 December 2020
Published: 23 December 2020

1. Introduction

The Great Plains receive much of their warm season precipitation from Mesoscale Convective Systems (MCSs) [1–5]. Nocturnal MCSs typically ingest buoyant air parcels from layers of air above the convectively stable PBL [6–9]. Agriculture in the central United States depends greatly on MCS rainfall events [1,10], and these events often bring severe weather [11,12]. Thus, accurately forecasting these events is important [13–16]. However, Quantitative Precipitation Forecasts (QPF) are very poor for summer precipitation from MCSs [17–20]. Jankov and Gallus [21] and Squitieri and Gallus [22], among others, found greater accuracy in forecasting precipitation events within strongly forced synoptic environments than in weakly forced ones. One reason for poor QPF skill with MCSs is displacement error in the simulated location. Duda and Gallus [23] and Squitieri and Gallus [24], for instance, found a 105 km average initiation displacement error for convection that often later evolved into MCSs, while Stelten and Gallus [25] found these errors to be between 77–105 km for multiple convection-allowing models run to support the Plains Elevated Convection At Night (PECAN) experiment.

The low-level jet (LLJ) plays a significant role in the initiation of MCSs, particularly during their growth and mature stages [6,26–31]. An LLJ can be loosely defined as a stream of fast-moving air, with low-level wind maxima of 10 to 30 ms^{-1}, and an elevation of the peak wind between 250 and 1000 m AGL [32]. The LLJ can be attributed to multiple factors, including an inertial oscillation [27,33] associated with changes in the diurnal cycle of surface heating [34] and boundary layer mixing, channeling of the winds by topography,

cold air pools and fronts, and heating-induced horizontal temperature gradients [35–37]. At the time of MCS initiation, the upstream region supplying inflow to the storms may not yet meet the Bonner [38] criteria for a LLJ, as MCS initiation often occurs earlier than LLJ development. While the flow may not yet meet LLJ criteria, the inflow region still is an important contributor to MCS development, as a terrain-heating/slope induced geostrophic low-level wind maximum [39] provides moisture and differential temperature advection to the region where an MCS initiates, along with convergence to develop and sustain the MCS.

Recent studies suggest that the amount of low-level moisture within a storm environment plays an influential role in where an MCS will initiate [24,40], and thus moisture errors within a simulation might explain some of the displacement errors present. A slight change in moisture at a parcel's lifted level may result in large changes in CAPE and CIN, bringing about various responses to the overall behavior of an MCS [41–43]. Peters et al. [40] showed for one MCS event during PECAN that in a region near and southwest of the MCS location, a smaller value of simulated CIN resulted in a small northeastward simulated MCS position error, while a large CIN resulted in a large northeastward simulated MCS position error, signifying the potential importance of low-level moisture supply on the location of MCS initiation within numerical weather prediction models. The simulated moisture regulated the time required for parcels to achieve convective initiation, with drier values hindering the buoyancy, resulting in a longer isentropic upglide distance for parcels to reach the level of free convection (LFC) and initiate convection.

Statistically significant correlations were discovered recently between the forecast accuracy of WRF (Weather Research and Forecasting) simulated LLJ thermodynamic variables and MCS QPF for strongly forced cases. Squitieri and Gallus [22] defined two synoptic environments in which MCSs associated with LLJs occur. Those with cyclonic flow aloft (at 200 hPa) and strong synoptic forcing were identified as Type C, and those with anticyclonic flow aloft and weak synoptic forcing were identified as Type A. In Type C cases, strong convergence was present at 900 hPa and coupled with 200 hPa divergence, while in Type A cases, little or no coupling of the 900 hPa convergence to the 200 hPa divergence was present. MCSs in Type A environments were forced by other, more diverse means. This coupling alongside the flow aloft was examined at 0600 UTC when the LLJ was usually most prominent [22].

Based on the findings of Peters et al. [40] for one MCS event, the present study seeks to find whether or not a strong statistical correlation exists between errors in several thermodynamic variables in the upstream inflow regions of initiating MCSs in simulations, and the spatial displacement errors of the simulated MCSs. In addition, because Squitieri and Gallus [22] found differing behaviors in cases with strongly forced versus weakly forced LLJ cases, the present study also explores sensitivity of the correlations to the amount of larger scale forcing. It is hypothesized that if negative (positive) simulated moisture errors exist in the inflow region for upscale growing convection, simulated MCSs will be displaced downstream (upstream) as more (less) lift would be required within the broad ascending airstream to bring parcels to their LFC, and that the greater the magnitude of the errors, the larger the displacements will be. Two approaches were taken when investigating these inflow regions. The first used the observed MCS initiation location at the time of initiation to explore the validity of the hypothesis. The second used inflow regions based on the position of the simulated MCS with the aim of finding a relationship to assist forecasting since the location of the observed MCS initiation would be unknown to forecasters in the hours preceding the event.

The paper is structured as follows. Section 2 describes the data used and methodology. Section 3 discusses statistical correlations and their significance and provides physical interpretation. Finally, Section 4 reviews relevant findings and outlines future work that could build upon the results.

2. Data and Methodology

2.1. MCS Events Examined

From the sample of 31 MCS events occurring over the eastern Great Plains and Midwest in the warm seasons of 2007–2014 and associated with LLJs examined in Squitieri and Gallus [22,24], 15 cases that had easily identifiable initiation locations and times were chosen, with 3 additional cases added from the 2015 PECAN project [44] that also met these criteria, to create a sample of 18 events. In all cases, relationships were examined between model forecast errors for specific humidity, equivalent potential temperature (θ_e), relative humidity, temperature, most unstable convective available potential energy (MUCAPE), most unstable convective inhibition (MUCIN), and the level of free convection (LFC) in the inflow regions of the upscale growing convection, and the spatial displacement errors present at the initiation of those MCSs. Because these cases included LLJs with MCS formation in the general region relative to the jet identified in the Maddox [45] climatology, it was assumed the inflow was gently ascending as suggested in that study, and shown in detail in the Peters et al. [40] MCS case. Additionally, one event was randomly chosen for a more thorough isentropic analysis, and it clearly showed the slowly ascending inflow into the region where MCS initiation took place. These parameters were selected based on the findings in Peters et al. [40] for one PECAN case and because parcel theory would suggest they could have a pronounced influence on convective initiation. The 18 cases were chosen based on the criterion that an MCS initiated in both model runs examined for each case, one run using the Yonsei University (YSU; [46]) PBL scheme, and the other using the Mellor-Yamada-Janjic (MYJ; [47]) PBL scheme. An equal number of 9 weakly forced cases where flow aloft was anticyclonically curved (Type A) and 9 strongly forced cases where flow aloft was cyclonic (Type C; see [21] for more details on classification of A and C events) were chosen for synoptic comparisons. Although the larger-scale environment in Type C events likely provided some of the forcing for the LLJ, LLJs in Type A events were likely primarily forced by the inertial oscillation, terrain sloping, or heating effects. Usually less lift via low-level convergence or upper level divergence was present for Type A cases than for Type C Cases [22].

2.2. Model Output

All of the events were simulated using WRF-ARW (Advanced Research WRF; [48]) version 3.6.1 with 3 km horizontal grid spacing. The Dudhia Shortwave [49] and RRTM Longwave [50] radiation schemes and the Thompson microphysics scheme [51] were used in all simulations, and no convective parameterization was used. The two PBL schemes used, YSU and MYJ, were chosen to explore the sensitivity of the simulated LLJs and MCSs to the PBL scheme choice. YSU is a nonlocal mixing scheme using first-order closure that represents entrainment at the top of the PBL and has been found to underestimate the LLJ wind magnitudes [52]. MYJ is a local mixing scheme using 1.5-order closure which used a prognostic calculation for turbulence with an equation for prognosis of TKE, with the addition of viscous sub-layer to the PBL through molecular diffusion, and may simulate environments that are too moist and cool, leading to overestimates of the low-level wind maximum [53]. The two PBL schemes were chosen due to their different behaviors, mainly related to the fact that one is local and the other is non-local, as well as the opposite magnitude errors they often have in simulating LLJs. For each case, the WRF was initialized at 12 UTC, roughly 12 h before MCS initiation, and runs were integrated for 24 h over a 1600 $\times$ 1600 km domain centered over the Great Plains (e.g., Figure 1), with 50 vertical levels (25 below 850 hPa, and 25 above). As explained in [22], this domain was generally centered over the LLJ and MCS of interest to keep the lateral boundaries as far from the area of interest as possible and reduce impacts related to lateral boundary conditions. 12 km NAM forecast output [54] was used to initialize the WRF and provide lateral boundary conditions.

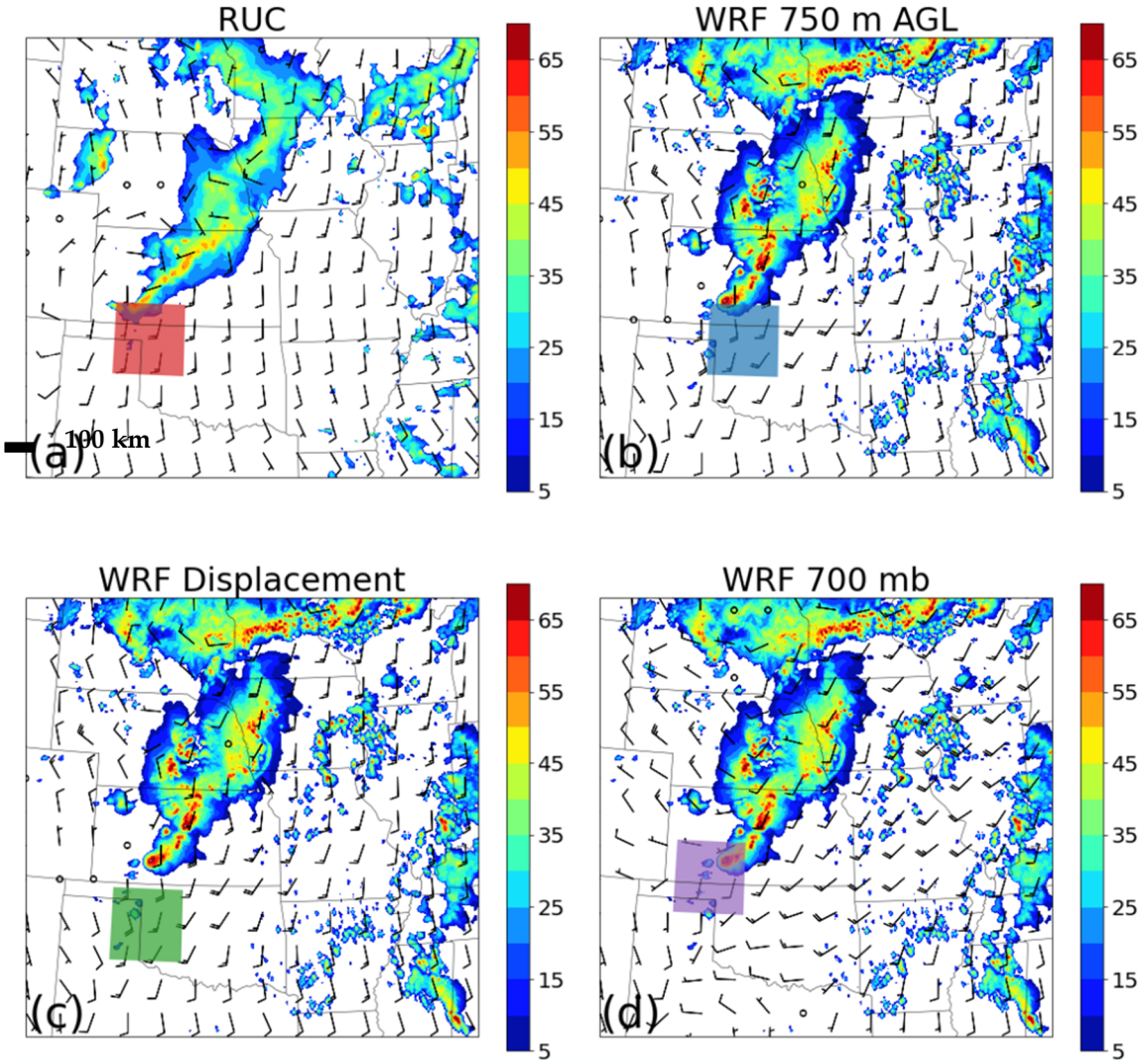

Figure 1. Type C case on 2 June 2014 at 0000 UTC showing all 4 regions used as inflow domains: (**a**) Obs-inflow (red), Rapid Update Cycle (RUC) 750 m AGL wind barbs, and observed mosaic composite reflectivity (see color bar for magnitudes), (**b**) Weather Research and Forecasting (WRF) 750m-inflow (blue), WRF 750 m AGL wind barbs, and simulated composite reflectivity, (**c**) WRFdisp (green), WRF 750 m AGL wind barbs, and simulated composite reflectivity, (**d**) WRF700mb-inflow (purple), WRF 700 mb wind barbs, and simulated composite reflectivity. Distance scale shown at bottom of (**a**).

As upper-air observations are scarce for nocturnal hours over the Great Plains, 0-h RUC or RAP analyses (RAP replaced RUC in 2012) with 13 km horizontal grid spacing were substituted for in-situ observational data [55], except for composite reflectivity. Past studies have explored the potential for biases to occur in RUC analyses, and have found that problems with using RUC output as a substitute for observational data were generally small, with errors close to the ranges for radiosonde accuracy [56]. Although forecasters do need to be aware of these errors, such analyses are the only high-resolution gridded depictions that exist of atmospheric variables above the surface, and thus RUC and RAP analyses have been used in place of observations in other synoptic and mesoscale studies (e.g., [22,24,57–60]). However, it should be noted that in the MCS case studied by Peters et al. [40], the RAP poorly represented the LLJ and moisture when compared to special PECAN soundings. Jahn and Gallus [61], on the other hand, found that for the full sample of LLJ cases in PECAN, RAP analyses of wind speed, potential temperature, and moisture generally matched PECAN soundings well, with only a small negative bias in wind speeds in the LLJ layer. In the present study, the RUC and RAP output, available every 25 hPa in the vertical, were interpolated to levels of constant height for comparisons with WRF output.

The WRF output was filtered using a Gaussian filter to remove waves with wavelengths less than 26 km (twice the 13 km grid spacing of the RAP and RUC output), and regridded to a 13-km horizontal grid to allow an appropriate comparison with the RAP and RUC data. Times and locations of MCS initiations (defined in the following sub-section) were identified using composite reflectivity from Multi-Radar Multi-Sensor (MRMS) 1-km hourly mosaic radar data [62], which were regridded to 3 km to match the WRF grid spacing for determination of the MCS initiation timing and location, and to a 13-km horizontal grid to match the grid spacing of the RAP and RUC analyses when used to determine points in the inflow that were convectively contaminated and removed (discussed in sub Section 2.4).

2.3. MCS Initiation and Inflow Region Identification

MCS initiation was identified using the criteria of Parker and Johnson [63] and Schumacher and Johnson [57]. Thus, an MCS was said to have initiated when a nearly-connected linear band of reflectivity greater than 40 dBZ, that may not show a reflectivity trough, exceeded 100 km in length. The initiation location was the centroid of the 40 dBZ echo region. Both of these criteria were evaluated subjectively. All cases contained an LLJ based on the Bonner [38] criteria, although at the time of MCS initiation, the flow within the inflow regions may not yet have met the criteria to be considered an LLJ (though all cases did reach LLJ criteria at some point during the night).

The inflow region was defined as a 250 km $\times$ 250 km domain for each case based on various levels of upstream wind flow using four different methods. It has long been shown (e.g., [45]) that MCSs develop near the nose of the LLJ with heat and moisture being supplied from a generally southerly direction, motivating our choice to focus on an inflow region. Our choice of a 250 km $\times$ 250 km domain was subjective, and we are unaware of prior works establishing what the best area would be over which to evaluate inflow characteristics. The first method evaluated 750 m AGL flow immediately upstream of the observed MCS initiation location (Figure 1a; hereafter referred to as Obs-inflow). This level was chosen as it is near or just above where the LLJ often peaks in intensity (e.g., [35,64]). Note that all of these inflow regions were chosen so that any overlap (at the inflow edge of the MCS) with the area of composite reflectivity greater than 40 dBZ was by less than 15%, with the majority of the inflow region extending upstream from that area of MCS initiation. The 750 m AGL flow at the time of MCS initiation was southerly in most cases, hence most inflow region sub-domains were located south of the MCS initiation point. Focusing on these regions allowed for the best evaluation of positive (negative) moisture errors in the inflow region of upscale growing convection that could systematically lead to upstream (downstream) displacement errors in the simulated MCS location. The second approach employed the same methodology as the first approach, but used the simulated MCS initiation location (Figure 1b; hereafter referred to as WRF750m-inflow), as correlations discovered using only model output could serve as a tool to allow forecasters to predict MCS spatial displacement errors. Using the observed MCS initiation location would not be possible in practice since forecasters would not know where an MCS would initiate in advance.

The third approach defined the inflow box using the simulated MCS initiation location but with an adjustment based on the average displacement errors of the simulated MCS initiations for the sample of cases examined in the present study (Figure 1c; hereafter referred to as WRFdisp). The average displacement errors for the runs using the YSU and MYJ schemes were 220 and 200 km, respectively. Because the simulated MCS initiations typically were north or northeast of the observed ones, the inflow regions were shifted 110 and 100 km south-southwest of the simulated MCS initiations, respectively. Only half of the average displacement distance was used to keep the domain relatively near and upstream of the simulated MCS initiation location.

The last approach allowed for the possibility that some events may feature displacement errors very different from the average and assumed that displacement errors may be related to the flow at some higher level for a given case. Because the 700 mb flow

direction often best matched the direction of the average displacement error, an inflow subdomain was chosen upstream of the simulated MCS initiation location with respect to the 700 mb flow (Figure 1d; hereafter referred to as WRF700mb-inflow). Both approaches three and four were investigated because correlations using an inflow region just upstream of the simulated MCS initiation (approach 2) were often much weaker than those obtained when using a region upstream of the observed MCS (approach 1). Inflow regions based on the WRF MCS initiation location with respect to both the 1500 m AGL flow and 500 mb flow were also studied, but the correlations were not as strong, and these results will not be discussed. It is acknowledged that these four inflow regions are defined subjectively, and future work could explore a much larger range of inflow regions systematically tested to find the area yielding strongest correlations. Within the four inflow regions on which this study will focus, thermodynamic variables within three vertical layers were studied, 250–750 m AGL (lower layer), 1000–1500 m AGL (upper layer), and 250–1500 m AGL (full layer).

2.4. Statistical Analysis Approach

Mean error was defined for the seven thermodynamic variables mentioned earlier for each inflow region and aforementioned vertical layers as the averaged WRF value over the inflow region subtracted from the averaged RUC value over the same inflow region. To minimize convective contamination of variables within the inflow regions, points within areas of reflectivity greater than 25 dBZ were ignored. The vector displacement error for MCS initiation location was calculated using the simulated MCS initiation location relative to observations. To gain further insight, correlations were also computed for the variables with the X and Y-components of displacement, which were calculated based on a rotated Cartesian axis with the Y-direction being parallel to the general wind direction in each inflow region, as seen in Figure 2 (positive Y-direction is upstream).

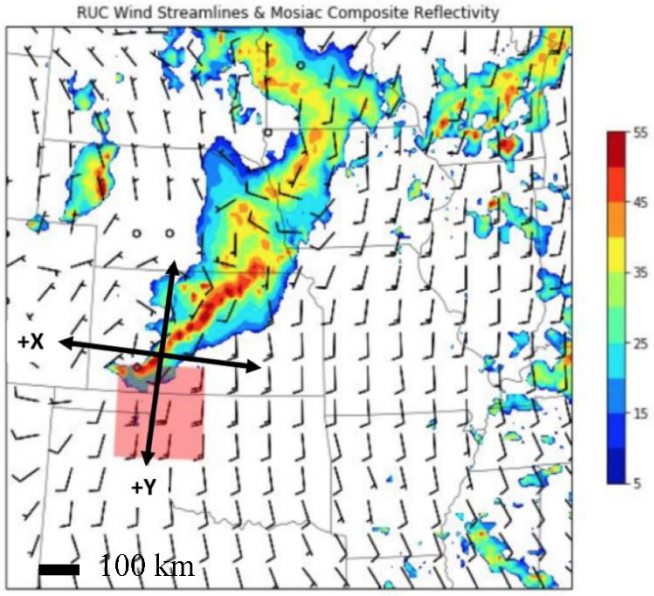

Figure 2. Mesoscale Convective System (MCS) case on 2 June 2014. Red area represents the Obs-inflow, and the axes represent the rotated coordinate system aligned with the 750 m AGL flow. Filled contours show mosaic composite reflectivity (dBZ as indicated by color bar), and RUC wind barbs are in m s^{-1}. Distance scale shown at lower left.

To determine the correlation between the errors in forecast thermodynamic variables and the MCS initiation displacement errors, the Spearman Rank Correlation (*S*) was employed. *S* was selected instead of the Pearson Correlation Coefficient to compensate for the small number of cases used in this study, as Type A and Type C cases were treated

separately. In addition to better handling small sample sizes, impacts of potential outlier cases (ones that may not follow any significant correlation) may be dampened with S, thus preserving statistical relationships between two variables that may otherwise be unfairly punished by an outlier [65]. S is also sign sensitive, and allows for the determination of statistical significance, making it a useful metric for the present study. Lastly, S is a non-parametric test, meaning it has statistical use for this study's data distribution as the mean errors and distance errors are statistically independent [65]. S was defined in Myers and Well [66] as:

$$S = 1 - \frac{6\sum_{i=1}^{n}(x_i - y_i)^2}{n(n^2-1)} \quad (1)$$

where n is the total number of samples, i is each case, and x_i and y_i are the ranks of the variables to be correlated, the mean errors of each tested variable and displacement of the initiating MCS, respectively. The 90th quantile of Spearman rank correlation values was used to determine statistical significance within this study's data to also compensate for the small sample size. Using a sample size of nine (as Type A and Type C cases are treated separately), the critical value for statistical significance was an absolute value of S greater than or equal to 0.4667, as determined by Conover ([65]; Table A10). For the cases analyzed in the present study, a positive S value usually signified that the more negative the errors in the thermodynamic variables, the greater the displacement error in the downstream (negative) direction, usually toward the northeast. A negative S value usually signified that as displacement errors became more negative, the mean errors were less negative (smaller in magnitude).

The calculations were done at four different times in hourly intervals. These included the time of initiation and the three hours prior to initiation. Although correlations were computed at all four times for all seven thermodynamic variables using all four inflow regions for both Type A and C cases, because the WRF750m-inflow region exhibited the weakest correlations of all regions investigated in this study, and the WRFdisp region mirrored the results from the WRF700mb-inflow region, with the latter having slightly higher significance values, the results that follow will focus only on correlations using the Obs-inflow and WRF700mb-inflow regions. In addition, because no significant correlations based on the 90th quantile were discovered using temperature, relative humidity, MUCIN, MUCAPE, or LFC, the discussion will focus primarily on specific humidity and θ_e. Although all of these parameters have an influence on convection, it is possible that for initiation, the most important ones are related to absolute moisture available around the specific inflow level, and not to other variables at that level, or parameters that reflect deeper layer conditions such as MUCIN or MUCAPE.

3. Results

3.1. Type C with YSU Scheme

In the Type C cases for WRF runs using the YSU scheme (Table 1), the Obs-inflow region showed statistically significant positive S values at nearly all times and in all 3 vertical layers with respect to the total spatial displacement of MCSs. This agrees with the hypothesis that errors in variables that would play a role in the level where saturation of an air parcel within ascending flow would occur will determine the displacement error of a simulated MCS. Positive S values were found in both specific humidity and θ_e. However, correlations at most times were not statistically significant for specific humidity with respect to the X and Y-components of displacement. θ_e showed a positive significant correlation at most times for all layers for the X-component as well as for the Y-component in the full layer. Both variables for all vertical layers contained similar positive statistical significance with respect to the total displacement but tended to diverge for the X and Y-components. An example scatterplot of the displacement errors associated with the errors in specific humidity at the time of initiation using the WRF700mb-inflow domain (Figure 3) reveals that the WRF almost always produced a drier low-level atmosphere upstream of the MCSs in the present sample of cases than what the RUC analyses showed. Negative moisture

errors were as large as 4 g kg^{-1} while positive errors generally remained no larger than roughly 1 g kg^{-1}. Because MCS initiation locations, and thus also displacement errors between the simulated locations and the observed ones, will not only be a function of the moisture fields, but also of other factors such as the position of zones of low-level convergence, and temperature fields, it is understandable that scatter exists in the plots in Figure 3, and that the relationships shown are not always monotonic.

Table 1. Spearman rank correlation coefficients (red indicates positive, blue negative) for all Type C cases simulated with WRF using the Yonsei University (YSU) scheme, and for all combinations of layers and displacements. Values are at time of initiation (t-0), and 3 h prior to time of initiation (t-3), and focus on two regions, the Obs-inflow region (RUC), and the WRF700mb-inflow region (WRF 700 mb). Bold font represents statistically significant correlations (S $\geq$ |0.467|), regular font not statistically significant correlations (S < |0.400|), and if a non-significant value was an outlier and the t-1 and t-2 values (which are not shown) were both significant, the value is indicated in italics.

Layer	**Specific Humidity**				**Equivalent Potential Temperature**				**Displacement**
	Obs-Inflow		**WRF700mb-Inflow**		**Obs-Inflow**		**WRF700mb-Inflow**		
	t-0	t-3	t-0	t-3	t-0	t-3	t-0	t-3	
Full Layer	**0.617**	**0.567**	**0.7**	**0.783**	**0.683**	**0.783**	**0.583**	**0.55**	Total Displacement
Lower Layer	*0.267*	**0.583**	**0.667**	**0.75**	**0.533**	**0.75**	**0.767**	**0.617**	
Upper Layer	*0.25*	**0.567**	**0.617**	**0.783**	*0.3*	**0.783**	*0.233*	**0.517**	
Full Layer	*0.433*	0.383	0.217	0.25	**0.5**	**0.6**	0.35	−0.1	X-Component
Lower Layer	**0.467**	*0.267*	**0.5**	0.3	**0.55**	*0.45*	0.267	0	
Upper Layer	0.05	**0.467**	0.167	0.167	*0.0067*	**0.6**	−0.05	−0.167	
Full Layer	0.333	*0.367*	**0.7**	**0.767**	**0.583**	**0.5**	**0.533**	**0.667**	Y-Component
Lower Layer	−0.117	0.433	**0.667**	**0.683**	*0.367*	**0.55**	**0.767**	**0.707**	
Upper Layer	0.217	0.3	**0.65**	**0.8**	*0.317*	**0.5**	*0.267*	**0.617**	

In the same set of Type C cases, the WRF700mb-inflow region followed the same trend for both variables for all vertical layers with respect to the total displacement values. Small differences existed from the values computed using Obs-inflow, but general results for both variables were similar. No significant S values were observed for the X-component at all layers, but the same significant positive correlation was present for all layers with respect to the Y-component. This set of Type C cases that were simulated using the YSU scheme had the most statistically significant S values with both inflow regions compared to the MYJ runs for Type C cases, and for both configurations with Type A cases as well, and showed the most consistency between all 3 vertical layers.

Significant positive correlations in both the total displacement and Y-component distances support the hypothesis that as negative moisture errors increase within a region, the simulated MCS will be displaced further downstream, and as the negative moisture error decreases, the simulated MCS will be nearer to the observed MCS with respect to the flow direction, as seen in Figure 4. This relationship suggests that if a positive moisture error existed in WRF, the MCS may initiate too far upstream, but since the present sample of cases rarely showed positive moisture errors, future work with a larger sample of cases is needed to verify this suggestion. For the X-component, a positive correlation means that as the negative moisture error increases, the simulated MCS will be displaced further to the right of the inflow direction. As will be discussed later, it is unclear why correlations existed with the X-component.

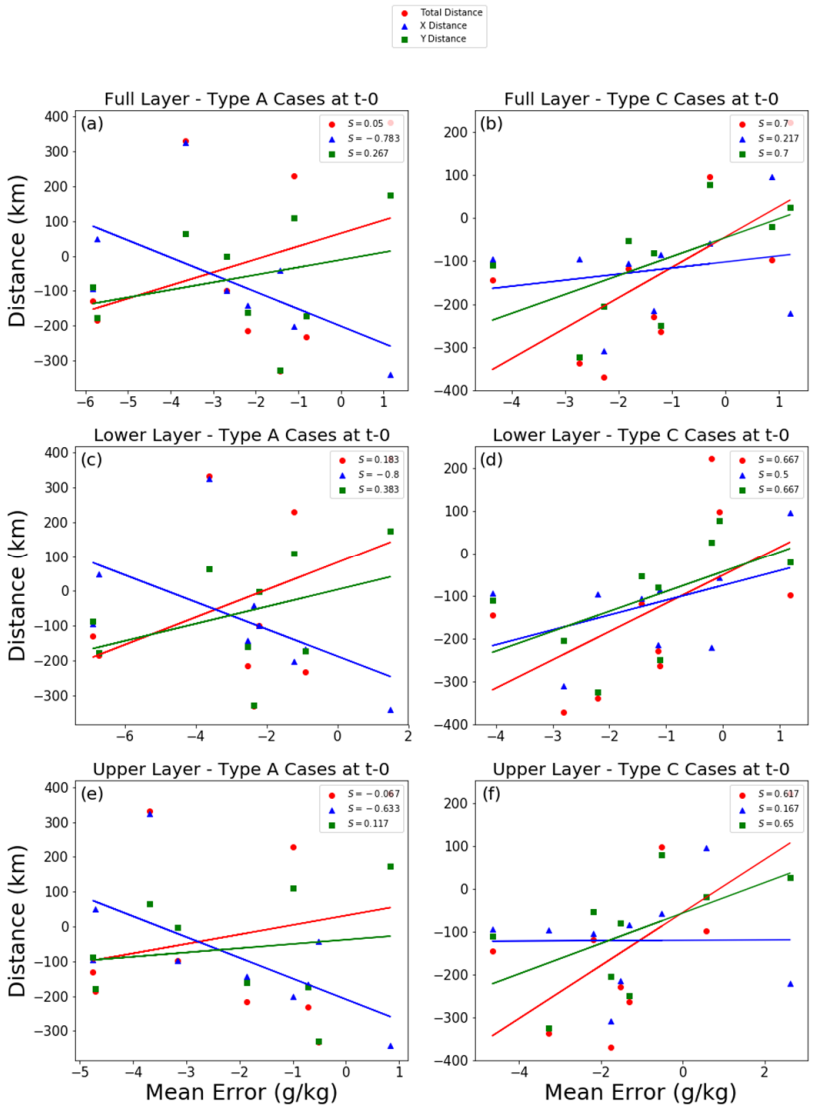

Figure 3. Scatterplots representing the correlations and their statistical significance for the WRF700mb-inflow region utilizing the YSU scheme. Specific humidity mean error is represented on the x-axis in g kg^{-1} and distance values on the y-axis are in km. Red circles represent the displacement error for MCS initiation locations, the blue triangles are their X-components of displacement, and the green squares Y-components of displacement. Spearman rank correlation coefficients are in the top-right corner with a line of best fit added to demonstrate the correlation behavior. (**a**) Full Layer-Type A Cases at t-0; (**b**) Full Layer-Type C Cases at t-0; (**c**) Lower Layer-Type A Cases at t-0; (**d**) Lower Layer -Type C Cases at t-0; (**e**)Upper Layer-Type A Cases at t-0; (**f**) Upper Layer-Type C Cases at t-0.

3.2. Type C with MYJ Scheme

With the MYJ PBL scheme in the WRF simulations, Type C cases differed more between vertical layers (Table 2). For specific humidity within the Obs-inflow region, only the lower layer contained significant positive correlations at most times for the total displacement and its X-component. However, the X-component was positively correlated for the full layer as well. This correlation was present for θ_e in the X-component, and for all vertical layers. For nearly all layers and the three displacement measures, the significance was larger at the earliest times, most removed from the time of initiation.

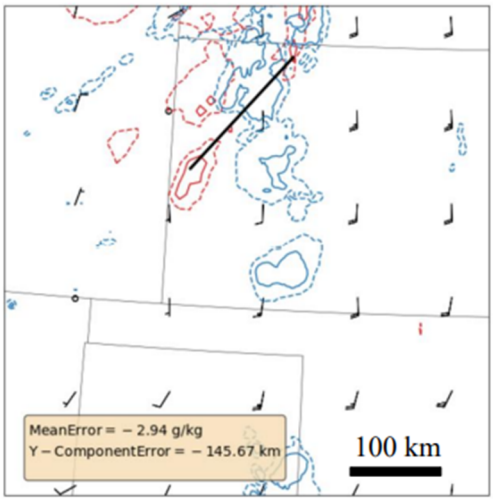

Figure 4. Type C case on 28 June 2014 at 0100 UTC, near the time of initiation. Red contours are mosaic composite reflectivity above 25 dBZ (dashed) and 40 dBZ (solid). Blue contours and wind barbs are WRF output with the Mellor-Yamada-Janjic (MYJ) scheme, with blue contours being composite reflectivity above 25 dBZ (dashed) and 40 dBZ (solid), and wind barbs representing the 750 m AGL wind. Bottom left corner displays the specific humidity mean error, and the Y-component displacement error (based on centroids of the 40 dBZ region), with the total displacement represented by the black line. Distance scale is shown in lower right.

Table 2. As in Table 1 except for WRF runs using MYJ.

Layer	Specific Humidity				Equivalent Potential Temperature				Displacement
	Obs-Inflow		WRF700mb-Inflow		Obs-Inflow		WRF700mb-Inflow		
	t-0	t-3	t-0	t-3	t-0	t-3	t-0	t-3	
Full Layer	0.15	0.433	**0.55**	**0.733**	0.233	**0.633**	*0.333*	**0.517**	Total Displacement
Lower Layer	*0.417*	**0.767**	**0.583**	**0.8**	0.2	**0.9**	**0.5**	**0.56**	
Upper Layer	−0.117	0.167	**0.467**	**0.65**	−0.217	0.45	0.15	0.45	
Full Layer	*0.367*	**0.633**	0.167	0.217	*0.417*	**0.667**	0.15	−0.033	X-Component
Lower Layer	**0.533**	**0.567**	**0.5**	*0.4*	*0.433*	**0.667**	0.3	0.1	
Upper Layer	−0.05	**0.5**	−0.017	0.15	*−0.15*	**0.683**	−0.333	−0.167	
Full Layer	0.117	−0.017	**0.617**	**0.633**	0.133	0.417	0.35	0.433	Y-Component
Lower Layer	0.0833	0.35	**0.75**	**0.617**	0.05	**0.683**	**0.467**	*0.4*	
Upper Layer	0.1	−0.05	**0.5**	**0.617**	0.15	0.15	0.167	0.433	

For the WRF700mb-inflow region, positive S values for specific humidity were observed at all layers with respect to the total displacement and its Y-component and were significant at nearly all times. There were also positive S values in the lower layer for its X-component, which are nearly identical to those observed using the YSU scheme. θ_e did not show as strong of correlations as specific humidity, but it also showed correlations were most significant at the earliest time, 3 h prior to initiation. However, significant positive correlations occurred at most times for the full layer with respect to the total displacement, as well as the lower layer for both the total displacement and its Y-component. Overall, the correlations for the MYJ runs were stronger in the lower layer than in the upper layer, while for the YSU runs, there was less difference in correlations between the two layers. Additionally, almost all S values were positive, signifying that simulated MCSs were displaced relatively consistently to the right and downstream when errors for both variables were negative, with larger displacements for larger errors. Although there was some variability in the S values with respect to each layer and inflow region used, the fact that the MYJ

runs had the most significant correlations confined to the lowest layer is consistent with the fact that the MYJ scheme is known to produce shallower PBLs than the YSU scheme, and these shallower PBLs are often cooler and more moist than those produced when the YSU scheme is used [53,67,68].

3.3. Type A with YSU Scheme

Table 3 shows the S values of correlations present for Type A cases that were simulated using the YSU scheme. The total displacement and its Y-component had significant positive correlations at most times within the full layer, but only the total displacement had significant positive correlations within the lower layer. This again agrees with results previously discussed for Type C cases that utilized both the YSU and MYJ schemes. However, significant negative correlations occurred within the full and upper layers with respect to the X-component. At most times, negative correlations were not observed in almost any Type C cases. These correlations are nearly mirrored for θ_e, apart from the full layer not showing statistically significant correlations for the X-component. The additional significant negative correlations occurred at most times. Within the WRF700mb-inflow region, the only significant correlations occurred for the X-component, and they were negative everywhere for both variables. Correlations were small and inconsistent for total displacements and Y-component distances. The negative correlations for the X-component were unexpected and are not addressed by the hypothesis. These negative correlations were associated with small negative moisture errors and large displacements to the right of the initiation location, and large negative moisture errors with little to no displacement to the right or left of the initiation location with respect to the inflow direction.

Table 3. As in Table 1 except for Type A cases.

Layer	Specific Humidity				Equivalent Potential Temperature				Displacement
	Obs-Inflow		WRF700mb-Inflow		Obs-Inflow		WRF700mb-Inflow		
	t-0	t-3	t-0	t-3	t-0	t-3	t-0	t-3	
Full Layer	**0.5**	*0.433*	0.05	−0.383	*0.417*	**0.483**	0.017	−0.167	Total Displacement
Lower Layer	**0.517**	**0.5**	0.183	−0.133	**0.583**	**0.55**	0.033	0.067	
Upper Layer	0.25	0.117	−0.067	**−0.583**	0.233	0.167	−0.1	**−0.517**	
Full Layer	*−0.33*	**−0.517**	**−0.783**	**−0.517**	−0.333	−0.417	**−0.65**	**−0.55**	X-Component
Lower Layer	−0.217	−0.133	**−0.8**	**−0.65**	−0.283	−0.183	**−0.683**	**−0.733**	
Upper Layer	**−0.55**	**−0.783**	**−0.633**	*−0.417*	**−0.517**	**−0.733**	**−0.617**	**−0.517**	
Full Layer	**0.48**	**0.467**	0.267	−0.2	0.367	**0.55**	0.2	0	Y-Component
Lower Layer	**0.467**	0.367	0.383	0.033	**0.583**	**0.5**	0.25	0.25	
Upper Layer	0.217	0.317	0.117	−0.367	0.183	0.417	0.067	−0.267	

The negative correlation with respect to the X-component was present for a majority of the Type A cases, with a good example depicted in Figure 5. Additional analysis was performed to try to understand why these negative correlations were present. Because Squitieri and Gallus [22] discovered some relationships between QPF skill and the depth and magnitude of the LLJ, these flow variables within the inflow regions, as well as MUCAPE, MUCIN, and LFC, were explored (Figures 6 and 7). Six cases were considered, three containing small negative moisture errors but a large rightward displacement (group 1), and three cases containing large negative moisture errors but little to no left or right displacement (group 2). Little difference was found in the LLJ variables between the two groups (Figure 6), and these results are mirrored in the other 3 inflow regions (figures not shown). Likewise, no differences were found in MUCAPE, MUCIN, and LFC between the two groups (Figure 7). These results are again mirrored by the other 3 inflow regions (figures not shown). Model errors in flow aloft, which would likely be veered from that used to define the inflow boxes in the present study, were also studied as these might

influence the X-component displacements. A preliminary analysis of 500 mb flow errors did not find systematic differences in the errors. In addition, the majority of surface maps for all Type A cases at 0000 UTC contained a nearby stationary front, usually with an east-west orientation, with southerly warm air blowing north towards colder air with easterly winds. Because Type A events are not associated with strong synoptic forcing, a variety of smaller-scale factors likely strongly influences the initiation and upscale growth of MCSs in those cases, and interactions between these factors may be complex. A detailed understanding of the reasons for the negative correlation would require a larger sample of cases and additional analysis beyond the scope of the present study.

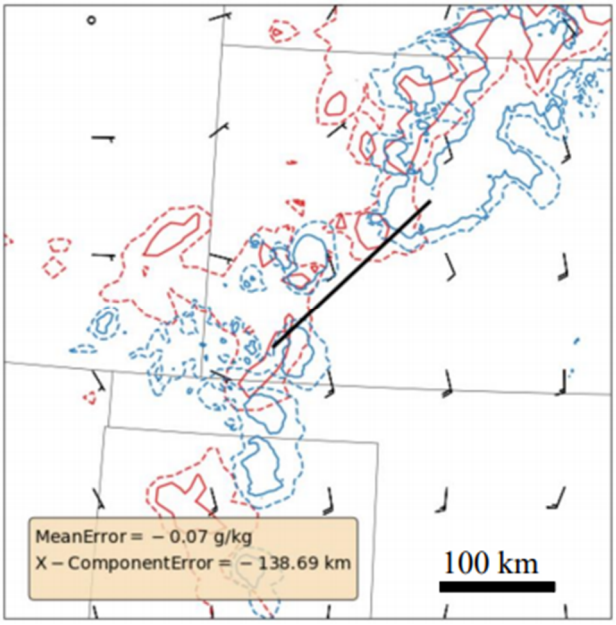

Figure 5. As in Figure 4, but for a Type A case on 15 June 2012 at 0000 UTC and showing the X-component error (km) instead of the Y-component displacement error in the box. Distance scale shown in lower right.

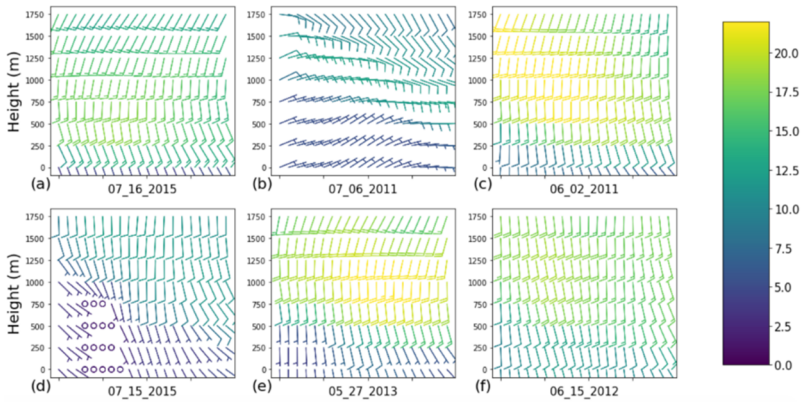

Figure 6. Low-level wind magnitude (ms^{-1}) and direction within the Obs-inflow region for six Type A cases (month, day, and year shown below each panel). Cross-section taken across the entire region from west to east at the halfway position from north to south across domain. Top row (**a**–**c**) are cases that contained a small X-component distance error, yet a large specific humidity mean error, while the bottom (**d**–**f**) are cases that contained a large X-component distance error, yet a small specific humidity mean error. Speeds indicated with color bar on the right.

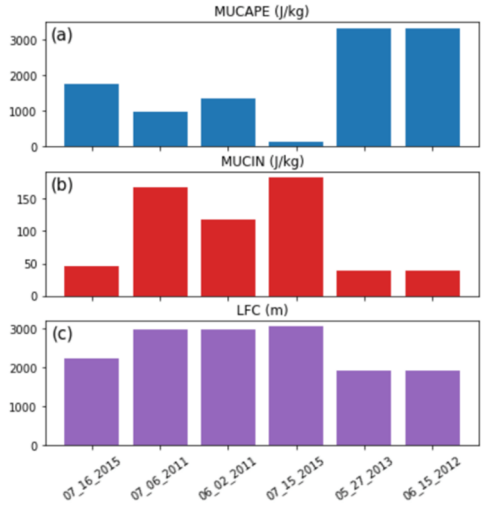

Figure 7. Most unstable CAPE (**a**), most unstable convective inhibition (MUCIN) (**b**), and level of free convection (LFC) height (**c**) within the inflow region for the same set of cases as in Figure 6, with top row of Figure 6 represented by the leftmost three dates, and bottom row represented by the rightmost three dates.

3.4. Type A with MYJ Scheme

Type A cases simulated with MYJ had the smallest number of significant S values in comparison to the other 3 scenarios examined (Table 4). For the Obs-inflow region, the lower layer contained significant positive S values at most times with respect to the total displacement. For the X-component, both the full and upper layers contained significant negative S values at most times, as was seen with the YSU output, and the results are mirrored identically for θ_e. The WRF700mb-inflow region contained almost no significant correlations for both variables. Individual times may have significant S values, but they do not remain consistent over the time period examined. The only strong correlation that existed at most times was for specific humidity with significant negative S values for the full layer with respect to the X-component.

Table 4. As in Table 2 except for Type A cases.

Layer	Specific Humidity				Equivalent Potential Temperature				Displacement
	Obs-Inflow		WRF700mb-Inflow		Obs-Inflow		WRF700mb-Inflow		
	t-0	t-3	t-0	t-3	t-0	t-3	t-0	t-3	
Full Layer	0.283	0.183	0.1	**−0.583**	0.25	0.0833	−0.033	**−0.517**	Total Displacement
Lower Layer	**0.483**	*0.433*	0.283	−0.133	**0.55**	*0.45*	0.033	−0.133	
Upper Layer	−0.033	0.05	−0.1	**−0.75**	0.133	0.0333	−0.117	**−0.617**	
Full Layer	**−0.567**	**−0.6**	**−0.517**	*−0.05*	**−0.6**	*−0.45*	−0.45	0.017	X-Component
Lower Layer	−0.183	−0.183	**−0.583**	−0.317	−0.267	−0.017	−0.4	−0.25	
Upper Layer	**−0.883**	**−0.683**	**−0.6**	0.117	**−0.817**	**−0.5**	**−0.517**	0.15	
Full Layer	0.267	0.267	0.217	**−0.5**	0.283	0.133	0.017	**−0.517**	Y-Component
Lower Layer	0.283	0.2	0.417	−0.05	0.4	0.183	0.1	−0.15	
Upper Layer	0.2	0.283	0	**−0.683**	0.367	0.2	−0.083	**−0.65**	

3.5. Application to Forecasting

Because positive correlations were common and often significant for Type C cases, even when an inflow domain was chosen based on the simulated MCS initiation location, forecasters may be able to use the information to anticipate a few hours ahead of time the displacement errors likely to be present for MCS initiation for these types of events.

Table 5 shows the layer and time with the most significantly positive value of S for specific humidity and θ_e, as this would be the best information for forecasters to use. Unfortunately, no systematic significant correlations dominated for Type A events using inflow determined from the simulated MCS initiation, so the present study cannot identify useful guidance for forecasters to anticipate displacement errors in advance for those events. Of note, since positive significant S values did exist at some times for some layers when using an inflow domain based on the observed MCS initiation, the general hypothesis still seems to be valid in these events, but none of the techniques tested in the present study was able to identify an inflow box that forecasters could use in advance of MCS initiation to predict displacement errors. The domain positions relative to the simulated initiating MCSs that worked well for Type C cases did not work for Type A cases.

Table 5. Largest positive Spearman rank correlation coefficients simulated in Type C cases using both MYJ and YSU schemes. S values were taken from the WRF700mb_inflow region and are shown for each displacement along with the time when valid.

Type	Moisture Variable	Displacement	S Value	Layer	Time
Type C	Specific Humidity	Total Displacement	0.8	Full, Lower	t-1, t-3
		X-Component	0.5	Lower	t-0, t-2
		Y-Component	0.8	Upper	t-3
	Equivalent Potential Temperature	Total Displacement	0.767	Lower	t-0
		X-Component	0.467	Lower	t-1
		Y-Component	0.767	Lower	t-0

4. Discussion and Conclusions

A set of 18 MCS events was examined to determine if errors in some thermodynamic variables within the inflow regions of MCSs were correlated well with spatial displacement errors present in the initiation stage of the MCSs. The MCSs were classified into two synoptic environments, Type C and A, based on the presence of strong and weak synoptic forcing, respectively. Prior studies [22,24] had found correlations that could assist forecasters were more common for Type C LLJ cases than for Type A LLJ cases, and forecast skill was greater for Type C events. Four inflow regions were used in the present study, with one based on the observed MCS initiation location and three others on the WRF simulated MCS initiation location. Three layers were examined, 250–750 m AGL, 1000–1500 m AGL, and 250–1500 m AGL. To determine the errors within the inflow region, WRF output was compared to RUC analyses. Correlations were then determined between these errors and the spatial displacements of the MCS initiations as well as their X and Y-components using a coordinate system defined by the direction of the inflow.

In Type C cases, as negative moisture errors increased, MCSs were displaced further downstream, agreeing with the findings of Peters et al. [40] for one PECAN case, and with the hypothesis that the location of MCS development is largely related to the level at which saturation would be reached within a broad ascending inflow layer. Significant positive correlations were observed for total displacement and its Y-component (in direction of the wind flow) for most of the Type C cases, and for the inflow region upstream of the observed MCS initiation for Type A cases. These results suggest that for Type C cases, forecasters may be able to use information on moisture errors a few hours prior to MCS initiation to estimate the displacement errors likely to be present for MCS initiation.

The strongest correlations for Type A cases were present for its X-component of displacement values, and the correlations were negative. These negative correlations mean that the larger the negative moisture errors, the closer the simulated MCS initiation was to the observed MCS initiation with respect to the left or right of the inflow direction. For a small negative moisture error, the simulated MCS initiation was displaced far to the right

of the observed initiating MCS. An analysis of multiple weather parameters was unable to explain the negative correlations. Due to the important role that numerous smaller-scale triggers play for Type A MCS initiation with the lack of strong synoptic forcing, it is difficult to identify a particular cause for the significant negative X-component correlation. It is also possible that with the small sample size, the negative correlations found in the present study may be more of a coincidence and may not be generalizable.

The present study also revealed the potential importance of the 700 mb flow in influencing the displacement of the simulated MCSs. It was recognized that to assist forecasters, an inflow region would need to be based on the simulated MCS initiation location and not that of the observed one. However, the WRF750 m-inflow region location performed much more poorly than Obs-inflow, without many significant correlations between errors there and the spatial displacement errors of the systems. An inflow box making use of the average displacement error from this small set of cases performed better. Because the average displacement direction matched rather well with the flow at 700 mb, an inflow box using 700 mb flow was also tested and found to result in the most significant correlations of all four regions explored. The fact that 700 mb worked well is consistent with the finding by Cotton et al. [26] that MCS initiation tends to occur in the region of maximum 700 mb warm air advection. Inflow boxes based on the 500 mb flow and flow at 1500 m AGL also were explored but yielded less significant correlations and smaller S values.

Some concerns may arise from the subjective approach to identifying the four inflow regions used in the present study. Regions were placed upstream of the MCS initiation location based on the direction of flow at several levels, and although areas of convective echoes were excluded, it is possible that convection altered some fields just outside these areas of reflectivity. Future work should more systematically examine a broader range of domain sizes, positions, and layers to find the best correlations. It is possible that an inflow domain could be found that would also provide forecasters with some ability to predict displacement errors for Type A cases. In addition, wind directions within the inflow box occasionally varied, such that there was some uncertainty in how to define the X and Y axes. Additionally, some of the cases in the present study occurred during the PECAN project in 2015 and a more thorough analysis could be performed in the future, using the high-temporal-frequency radiosonde launches from PECAN as done in Peters et al. [40] instead of RUC analyses alone. In addition, the present study focused on the initiation stage of an MCS. A similar study could be performed at a later stage in the life cycle of MCSs, perhaps when the inflow region truly represents the flow of a well-developed LLJ. Would displacement errors for mature MCSs correlate well with errors within the strong LLJs? Although documentation of such a relationship may be less useful to forecasters prior to the time of MCS initiation, if such a relationship exists, forecasters might be able to use analyses during the time the LLJ develops to adjust model predictions of where an MCS would be during its mature stage, based on moisture errors, for instance, that are showing up within the LLJ during its development. This information may also be useful to flood forecasters since a large portion of rainfall happens during the mature stage of a MCS.

Author Contributions: Conceptualization and methodology N.J.V. and W.A.G.J.; software, N.J.V.; validation, N.J.V. and W.A.G.J.; formal analysis, N.J.V.; resources, N.J.V., W.A.G.J., and B.J.S.; data curation, N.J.V. and B.J.S.; writing—original draft preparation, N.J.V.; writing—review and editing, N.J.V., W.A.G.J., and B.J.S.; supervision, W.A.G.J.; project administration, W.A.G.J.; funding acquisition, W.A.G.J. All authors have read and agreed to the published version of the manuscript.

Funding: This work was funded by NSF Awards AGS1624947 and AGS2022888.

Acknowledgments: We would like to acknowledge high-performance computing support from Yellowstone (ark:/85065/d7wd3xhc) provided by NCAR's Computational and Information Systems Laboratory, sponsored by the National Science Foundation, for the WRF simulations used in the present study. The authors would like to extend thanks to Daryl Herzmann for assistance with

all Python implementations utilized. The constructive comments of three anonymous reviewers strengthened the paper.

Conflicts of Interest: The authors declare no conflict of interest.

References

1. Fritsch, J.M.; Kane, R.J.; Chelius, C.R. The contribution of mesoscale convective weather systems to warm season precipitation in the united states. *J. Appl. Meteor.* **1986**, *25*, 1333–1345. [CrossRef]
2. Ashley, W.S.; Mote, T.L.; Dixon, P.G.; Trotter, S.L.; Powell, E.J.; Durkee, J.D.; Grundstein, A.J. Distribution of mesoscale convective complex rainfall in the US. *Mon. Weather Rev.* **2003**, *131*, 3003–3017. [CrossRef]
3. Carbone, R.E.; Tuttle, J.D. Rainfall occurrence in the U.S. warm season: The diurnal cycle. *J. Clim.* **2008**, *21*, 4132–4146. [CrossRef]
4. Haberlie, A.M.; Ashley, W.A. A radar-based climatology of mesoscale convective systems in the US. *J. Clim.* **2019**, *32*, 1591–1606. [CrossRef]
5. Feng, Z.; Houze, R.A., Jr.; Leung, L.R.; Song, F.; Hardin, J.C.; Wang, J.; Gustafson, W.I., Jr.; Homeyer, C.R. Spatiotemporal characteristics and large-scale environments of mesoscale convective systems east of the Rocky Mountains. *J. Clim.* **2019**, *32*, 7303–7328. [CrossRef]
6. Trier, S.B.; Parsons, D.B. Evolution of environmental conditions preceding the development of a nocturnal mesoscale convective complex. *Mon. Weather Rev.* **1993**, *121*, 1078–1098. [CrossRef]
7. Moore, J.T.; Glass, F.H.; Graves, C.E.; Rochette, S.M.; Singer, M.J. The environment of warm-season elevated thunderstorms associated with heavy rainfall over the central USA. *Weather Forecast.* **2003**, *18*, 861–878. [CrossRef]
8. Horgan, K.L.; Schultz, D.M.; Hales, J.E.; Corfidi, S.F.; Johns, R.H. A five-year climatology of elevated severe convective storms in the US East of the Rocky Mountains. *Weather Forecast.* **2007**, *22*, 1031–1044. [CrossRef]
9. Corfidi, S.F.; Corfidi, S.J.; Schultz, D.M. Elevated convection and castellanus: Ambiguities, significance, and questions. *Weather Forecast.* **2008**, *23*, 1280–1303. [CrossRef]
10. Ahijevych, D.; Pinto, J.O.; Williams, J.K.; Steiner, M. Probabilistic forecasts of mesoscale convective system initiation using the random forest data mining technique. *Weather Forecast.* **2016**, *31*, 581–599. [CrossRef]
11. Gallus, W.A., Jr.; Snook, N.A.; Johnson, E.V. Spring and summer severe weather reports over the Midwest as a function of convective mode: A preliminary study. *Weather Forecast.* **2008**, *23*, 101–113. [CrossRef]
12. Hocker, J.E.; Basara, J.B. A 10-year spatial climatology of squall line storms across Oklahoma. *Int. J. Climatol.* **2008**, *28*, 765–775. [CrossRef]
13. Jirak, I.L.; Cotton, W.R. Observational analysis and predictability of mesoscale convective systems. *Weather Forecast.* **2007**, *22*, 813–838. [CrossRef]
14. Jirak, I.L.; Cotton, W.R.; McAnelly, R.L. Satellite and radar survey of mesoscale convective system development. *Mon. Weather Rev.* **2003**, *131*, 2428–2449. [CrossRef]
15. Stensrud, D.J.; Wicker, L.J.; Xue, M.; Dawson, D.T., II; Yussouf, N.; Wheatley, D.M.; Thompson, T.E.; Snook, N.A.; Smith, T.M.; Schenkman, A.D.; et al. Progress and challenges with warn-on-forecast. *Atmos. Res.* **2013**, *123*, 2–16. [CrossRef]
16. Pinto, J.O.; Grim, J.A.; Steiner, M. Assessment of the high-resolution rapid refresh model's ability to predict mesoscale convective systems using object-based evaluation. *Weather Forecast.* **2015**, *30*, 892–913. [CrossRef]
17. Stensrud, D.J.; Fritsch, J.M. Mesoscale convective systems in weakly forced large-scale environments. Part III: Numerical simulations and implications for operational forecasting. *Mon. Weather Rev.* **1994**, *122*, 2084–2104. [CrossRef]
18. Gallus, W.A., Jr. Impact of verification grid-box size on warm-season QPF skill measures. *Weather Forecast.* **2002**, *17*, 1296–1302. [CrossRef]
19. Davis, C.A.; Manning, K.W.; Carbone, R.E.; Trier, S.B.; Tuttle, J.D. Coherence of warm-season continental rainfall in numerical weather prediction models. *Mon. Weather Rev.* **2003**, *131*, 2667–2679. [CrossRef]
20. Gallus, W.A., Jr. Rainfall Forecasting. The challenge of warm-season convective precipitation forecasting. In *Hydrological Science and Engineering*; Wong, T.S.W., Ed.; Nova Science Publishers: Hauppauge, NY, USA, 2012; pp. 129–160. ISBN 978-61942-134-9.
21. Jankov, I.; Gallus, W.A., Jr. MCS rainfall forecast accuracy as a function of large-scale forcing. *Weather Forecast.* **2004**, *19*, 428–439. [CrossRef]
22. Squitieri, B.J.; Gallus, W.A., Jr. WRF forecasts of Great plains nocturnal low-level jet-driven MCSs. Part I: Correlation between low-level jet forecast accuracy and MCS precipitation forecast skill. *Weather Forecast.* **2016**, *31*, 1301–1323. [CrossRef]
23. Duda, J.D.; Gallus, W.A., Jr. The impact of large-scale forcing on skill of simulated convective initiation and upscale evolution with convection-allowing grid spacings in the WRF. *Weather Forecast.* **2013**, *28*, 994–1018. [CrossRef]
24. Squitieri, B.J.; Gallus, W.A., Jr. WRF forecasts of Great plains nocturnal low-level jet-driven MCSS. Part II: Differences between strongly and weakly forced low-level jet environments. *Weather Forecast.* **2016**, *31*, 1491–1510. [CrossRef]
25. Stelten, S.; Gallus, W.A., Jr. Pristine nocturnal convective initiation: A climatology and preliminary examination of predictability. *Weather Forecast.* **2017**, *32*, 1613–1635. [CrossRef]
26. Cotton, W.R.; Lin, M.S.; McAnelly, R.L.; Tremback, C.J. A composite model of mesoscale convective complexes. *Mon. Weather Rev.* **1989**, *117*, 765–783. [CrossRef]
27. Augustine, J.A.; Caracena, F. Lower-tropospheric precursors to nocturnal MCS development over the central United States. *Weather Forecast.* **1994**, *9*, 116–135. [CrossRef]

28. Mitchell, M.J.; Arritt, R.W.; Labas, K. A climatology of the warm season Great Plains low-level jet using wind profiler observations. *Weather Forecast.* **1995**, *10*, 576–591. [CrossRef]
29. Higgins, R.W.; Yao, Y.; Yarosh, E.S.; Janowiak, J.E.; Mo, K.C. Influence of the Great Plains low-level jet on summertime precipitation and moisture transport over the central US. *J. Clim.* **1997**, *10*, 481–507. [CrossRef]
30. Trier, S.B.; Davis, C.A.; Ahijevych, D.A.; Weisman, M.L.; Bryan, G.H. Mechanisms supporting long-lived episodes of propagating nocturnal convection within a 7-day WRF model simulation. *J. Atmos. Sci.* **2006**, *63*, 2437–2461. [CrossRef]
31. French, A.J.; Parker, M.D. The response of simulated nocturnal convective systems to a developing low-level jet. *J. Atmos. Sci.* **2010**, *67*, 3384–3408. [CrossRef]
32. Stull, R.H. *An Introduction to Boundary Layer Meteorology*; Kluwer Academic Publishers: Dordrecht, The Netherlands, 1988; 666p.
33. Blackadar, A.K. Boundary layer wind maxima and their significance for the growth of nocturnal inversions. *Bull. Amer. Meteor. Soc.* **1957**, *38*, 283–290. [CrossRef]
34. Bonner, W.D.; Paegle, J. Diurnal variations in boundary layer winds over the south-central US in summer. *Mon. Weather Rev.* **1970**, *98*, 735–744. [CrossRef]
35. Stensrud, D.J. Importance of low-level jets to climate: A Review. *J. Clim.* **1996**, *9*, 1698–1711. [CrossRef]
36. Berg, L.K.; Riihimaki, L.D.; Qian, Y.; Yan, H.; Huang, M. The low-level jet over the southern Great Plains determined from observations and reanalyses and its impact on moisture transport. *J. Clim.* **2015**, *28*, 6682–6706. [CrossRef]
37. Shapiro, A.; Fedorovich, E.; Rahimi, S. A unified theory for the Great Plains nocturnal low-level jet. *J. Atmos. Sci.* **2016**, *73*, 3037–3057. [CrossRef]
38. Bonner, W.D. Climatology of the low level jet. *Mon. Weather Rev.* **1968**, *96*, 833–850. [CrossRef]
39. Parish, T.R.; Oolman, L.D. On the role of sloping terrain in the forcing of the Great Plains low-level jet. *J. Atmos. Sci.* **2010**, *67*, 2690–2699. [CrossRef]
40. Peters, J.M.; Nielsen, E.R.; Parker, M.D.; Hitchcock, S.M.; Schumacher, R.S. The impact of low-level moisture errors on model forecasts of an MCS observed during PECAN. *Mon. Weather Rev.* **2017**, *145*, 3599–3624. [CrossRef]
41. Thompson, R.L.; Mead, C.M.; Edwards, R. Effective storm-relative helicity and bulk shear in supercell thunderstorm environments. *Weather Forecast.* **2007**, *22*, 102–115. [CrossRef]
42. Schumacher, R.S. Sensitivity of precipitation accumulation in elevated convective systems to small changes in low-level moisture. *J. Atmos. Sci.* **2015**, *72*, 2507–2524. [CrossRef]
43. Schumacher, R.S.; Peters, J.M. Near-surface thermodynamic sensitivities in simulated extreme-rain-producing mesoscale convective systems. *Mon. Weather Rev.* **2017**, *145*, 2177–2200. [CrossRef]
44. Geerts, B.; Parsons, D.; Ziegler, C.L.; Weckwerth, T.M.; Biggerstaff, M.I.; Clark, R.D.; Coniglio, M.C.; Demoz, B.B.; Ferrare, R.A.; Gallus, W.A., Jr.; et al. The 2015 plains elevated convection at night field project. *Bull. Amer. Meteor. Soc.* **2017**, *98*, 767–786. [CrossRef]
45. Maddox, R.A. Large-scale meteorological conditions associated with midlatitude, mesoscale convective complexes. *Mon. Weather Rev.* **1983**, *111*, 1475–1493. [CrossRef]
46. Hong, S.Y.; Noh, Y.; Dudhia, J. A new vertical diffusion package with an explicit treatment of entrainment processes. *Mon. Weather Rev.* **2006**, *134*, 2318–2341. [CrossRef]
47. Janjić, Z.I. The step-mountain eta coordinate model: Further developments of the convection, viscous sublayer, and turbulence closure schemes. *Mon. Weather Rev.* **1994**, *122*, 927–945. [CrossRef]
48. Skamarock, W.C.; Klemp, J.B.; Dudhia, J.; Gill, D.O.; Barker, D.; Duda, M.G.; Powers, J.G. *A Description of the Advanced Research WRF v3*; Citeseer: Boulder, CO, USA, 2008.
49. Dudhia, J. Numerical study of convection observed during the winter monsoon experiment using a mesoscale two-dimensional model. *J. Atmos. Sci.* **1989**, *46*, 3077–3107. [CrossRef]
50. Mlawer, E.J.; Taubman, S.J.; Brown, P.D.; Iacono, M.J.; Clough, S.A. Radiative transfer for inhomogeneous atmospheres: RRTM, a validated correlated-k model for the longwave. *J. Geophys. Res.* **1997**, *102*, 16663–16682. [CrossRef]
51. Thompson, G.; Field, P.R.; Rasmussen, R.M.; Hall, W.D. Explicit forecasts of winter precipitation using an improved bulk microphysics scheme. Part II: Implementation of a new snow parameterization. *Mon. Weather Rev.* **2008**, *136*, 5095–5115. [CrossRef]
52. Smith, E.N.; Gibbs, J.A.; Fedorovich, E.; Klein, P.M. WRF Model study of the Great Plains low-level jet: Effects of grid spacing and boundary layer parameterization. *J. Appl. Meteor. Climatol.* **2018**, *57*, 2375–2397. [CrossRef]
53. Schumacher, R.S.; Clark, A.J.; Xue, M.; Kong, F. Factors influencing the development and maintenance of nocturnal heavy-rain-producing convective systems in a storm scale ensemble. *Mon. Weather Rev.* **2013**, *141*, 2778–2801. [CrossRef]
54. NOAA/National Climatic Data Center. NCEP Numerical Weather Prediction Models North American. Available online: http://nomads.ncdc.noaa.gov/cgi-bin/ncdcui/definecollection.pl?model_sys=nam&model_name=nam&grid_name=MesoScaleGrid218 (accessed on 23 February 2015).
55. NOAA/National Climatic Data Center. NCEP Rapid Update Cycle (13 km RUC). Available online: nomads.ncdc.noaa.gov/data/ruc13/ (accessed on 23 February 2015).
56. Thompson, R.L.; Edwards, R.; Hart, J.A.; Elmore, K.L.; Markowski, P.M. Close proximity sounding within supercell environments obtained from the Rapid Update Cycle. *Weather Forecast.* **2003**, *18*, 1243–1261. [CrossRef]
57. Schumacher, R.S.; Johnson, R.H. Organization and environmental properties of extreme-rain-producing mesoscale convective systems. *Mon. Weather Rev.* **2005**, *133*, 961–976. [CrossRef]

58. Hane, C.E.; Haynes, J.A.; Andra, D.L.; Carr, F.H. The evolution of morning convective systems over the U. S. Great Plains during the warm season. Part II: A climatology and the influence of environmental factors. *Mon. Weather Rev.* **2008**, *136*, 929–944. [CrossRef]
59. Coniglio, M.C.; Hwang, J.Y.; Stensrud, D.J. Environmental factors in the upscale growth and longevity of MCSs derived from the rapid update cycle analyses. *Mon. Weather Rev.* **2010**, *138*, 3514–3539. [CrossRef]
60. Snively, D.V.; Gallus, W.A., Jr. Prediction of convective morphology in near-cloud-permitting WRF model simulations. *Weather Forecast.* **2014**, *29*, 130–149. [CrossRef]
61. Jahn, D.E.; Gallus, W.A., Jr. Impacts of modifications to a local planetary boundary layer scheme on forecasts of the Great Plains low-level jet environment. *Weather Forecast.* **2018**, *33*, 1109–1120. [CrossRef]
62. Smith, T.M.; Lakshmanan, V.; Stumpf, G.J.; Ortega, K.L.; Hondl, K.; Cooper, K.; Calhoun, K.M.; Kingfield, D.M.; Manross, K.L.; Toomey, R.; et al. Multi-radar multi-sensor (MRMS) severe weather and aviation products: Initial operating capabilities. *Bull. Am. Meteor. Soc.* **2016**, *97*, 1617–1630. [CrossRef]
63. Parker, M.D.; Johnson, R.H. Organizational modes of midlatitude mesoscale convective systems. *Mon. Wea. Rev.* **2000**, *128*, 3413–3436. [CrossRef]
64. Parish, T.R. On the forcing of the summertime Great Plains Low-Level Jet. *J. Atmos. Sci.* **2017**, *74*, 3937–3953. [CrossRef]
65. Conover, W.J. *Practical Nonparametric Statistics*, 2nd ed.; John Wiley and Sons: Hoboken, NJ, USA, 1971; 493p.
66. Myers, J.L.; Well, A.D. *Research Design and Statistical Analysis*, 2nd ed.; Chapman and Hall: London, UK, 2003; 508p.
67. Hu, X.; Nielsen-Gammon, J.W.; Zhang, F. Evaluation of three planetary boundary layer schemes in the WRF model. *J. Appl. Meteor. Climatol.* **2010**, *49*, 1831–1844. [CrossRef]
68. Coniglio, M.C.; Correia, J.; Marsh, P.T.; Kong, F. Verification of convection-allowing WRF model forecasts of the planetary boundary layer using sounding observations. *Weather Forecast.* **2013**, *28*, 842–862. [CrossRef]